Ore Geology Reviews 135 (2021) 104194

Contents lists available at ScienceDirect

Ore Geology Reviews

journal homepage: www.elsevier.com/locate/oregeorev

3D geostatistical modeling of metal contents and lithofacies for mineralization mechanism determination of a seafloor hydrothermal deposit in the middle Okinawa Trough, Izena Hole

Vitor Ribeiro de Sá [a], Katsuaki Koike [a,*], Tada-nori Goto [b], Tatsuo Nozaki [c,d,e,f], Yutaro Takaya [c,f,g,h], Toru Yamasaki [i]

[a] Department of Urban Management, Graduate School of Engineering, Kyoto University, Kyoto 615-8540, Japan
[b] Graduate School of Life Science, University of Hyogo, Himeji, Hyogo 671-2280, Japan
[c] Submarine Resources Research Center, Research Institute for Marine Resources Utilization, Japan Agency for Marine-Earth Science and Technology (JAMSTEC), Yokosuka, Kanagawa 237-0061, Japan
[d] Frontier Research Center for Energy and Resources (FRCER), School of Engineering, The University of Tokyo, Tokyo 113-8656, Japan
[e] Department of Planetology, Graduate School of Science, Kobe University, Kobe, Hyogo 657-8501, Japan
[f] Ocean Resources Research Center for Next Generation, Chiba Institute of Technology, Narashino, Chiba 275-0016, Japan
[g] Department of Systems Innovation, Faculty of Engineering, University of Tokyo, Tokyo 113-8656, Japan
[h] Faculty of Science and Engineering, Waseda University, Tokyo 169-8555, Japan
[i] Research Institute of Geology and Geoinformation, Geological Survey of Japan (AIST), Tsukuba, Ibaraki 305-8567, Japan

ARTICLE INFO

Keywords:
Seafloor hydrothermal deposits
Geochemical composition
Principal component analysis
Cluster analysis
3D geologic model
Pluri-Gaussian simulation

ABSTRACT

Seafloor hydrothermal deposits in the Okinawa Trough have been regarded as a modern analog of kuroko-type volcanogenic massive sulfide (VMS) deposits on land. VMS deposit is one of the primary producers of base metals (e.g. Cu, Pb, Zn) and precious metals (e.g. Au, Ag). However, owing to difficulties in accessing subseafloor samples/data without costly drilling operations, the spatial distribution of metal contents below the seafloor remains poorly constrained. We apply a combination of four spatial modeling methods: (1) principal component analysis; (2) k-means clustering; and (3, 4) conditional geostatistical simulations of turning bands and pluri-Gaussian. These modeling methods are based on the whole-rock geochemical data using inductively coupled plasma-quadruple mass spectrometry, together with lithologic log data obtained from onboard visual core descriptions, and X-ray diffraction analyses from the middle Okinawa Trough, Izena Hole, during the cruise CK16-05 (Expedition 909) in 2016 by *D/V Chikyu*. The primary goal is to construct plausible 3D models for the contents of base metals and silver as well as lithotypes. The constructed models successfully map the configuration and zonation of subseafloor metal deposits with hydrothermal flow paths, which sheds light on hydrothermal circulation systems and metal accumulation mechanisms. This approach is shown to be effective for geologic and mineralization modeling and exploration of (sub)seafloor hydrothermal deposits.

1. Introduction

Submarine mineral resources (e.g. seafloor massive sulfide (SMS) deposits, Fe-Mn nodules, Fe-Mn crusts, and REY (rare earth element- and yttrium)-rich muds) have attracted considerable economic interest as a new resource with particularly large resources (Kato et al., 2011; Hein et al., 2013; Masuda et al., 2014; Takaya et al., 2018). Seafloor hydrothermal deposits have been the focus of extensive research since the late 1960 s particularly with regards to the relationship between distribution, mineralization mechanisms, and hydrothermal flux cycles (e.g. Degens and Ross, 1969; Hutchinson, 1973; Sawkins, 1976; Cox and Singer, 1986; Poulsen and Hannington, 1995; Herzig and Hannington, 1995; Glasby and Notsu, 2003; Galley et al., 2007; Ishibashi et al., 2015) largely because SMS deposits may be future producers of Cu, Zn, Pb, Au, and Ag resources (Hannington et al., 2011; Shanks and Thurston, 2012; Singer, 2014; Juliani and Ellefmo, 2018a, 2018b, 2019). Although geological, geochemical, and geophysical data can be collected from the seafloor from dive surveys, the subseafloor structure, metallogenesis,

* Corresponding author.
E-mail address: koike.katsuaki.5x@kyoto-u.ac.jp (K. Koike).

https://doi.org/10.1016/j.oregeorev.2021.104194
Received 5 March 2020; Received in revised form 29 March 2021; Accepted 21 April 2021
Available online 25 April 2021

and metal element distributions of SMS deposits remain poorly understood owing to difficulties involved with accessing subseafloor samples/data without costly drilling operations.

To address this problem and extract more information from sparse drilling data, we apply a combination of data-characterization methods using principal component analysis (PCA), k-means clustering, conditional geostatistical simulations of turning bands (TBSIM), and pluri-Gaussian (PGSIM). A merit of TBSIM, which simulates the 2D or 3D domain by yielding a series of one-dimensional simulations along lines in $\mathbb{R}^n$ (Emery and Lantuéjoul, 2006), is its versatility and low CPU cost (Olea, 1999; Hunger et al., 2015; Marcotte, 2016). Its availability for SMS deposits was demonstrated in our previous study to delineate features of subseafloor stockworks and strata-bound mineralization (de Sá et al., 2020). The effectiveness of PGSIM has been demonstrated to produce realistic geologic models with complex patterns by honoring stratigraphic rules, such as the relative positions and proportions of different lithotypes over a wide range (Mariethez et al., 2009; Armstrong et al., 2011).

The primary goal is to construct plausible 3D models of geochemical compositions and lithotypes at the Hakurei Site, Izena Hole (Ishibashi et al., 2014; Totsuka et al., 2019; Morozumi et al., 2020; Nozaki et al., 2021a) where the largest SMS deposit in the Okinawa Trough is used as a case field study (Fig. 1). SMS deposits in the Okinawa Trough have been considered a modern analog of kuroko-type volcanogenic massive sulfide (VMS) deposits on land (Halbach et al., 1989, 1993; Pirajno, 2009; Ishibashi et al., 2015; Nozaki et al., 2016). We use whole-rock geochemical data of drill core samples together with lithological information based on onboard visual core descriptions and X-ray diffraction (XRD) analyses at six drill sites obtained from the cruise CK16-05 (Expedition 909) in 2016 by *D/V Chikyu* (Nozaki et al., 2021b). Whole-rock geochemical data are determined by inductively coupled plasma-quadrupole mass spectrometry (ICP-QMS) using the HF-HNO_3-$HClO_4$ acid digestion method (Takaya et al., 2018). To compensate for the sparse geochemical data, a seismic profile (Fig. 1d) is incorporated to interpret the subseafloor geologic structure. Kuroko-type VMS deposits on land are well-studied analogs of SMS deposits and can provide useful information, particularly 3D studies of the Hokuroku District in northeast Japan (e.g. Cathles, 1983; Date et al., 1983; Eldridge et al., 1983; HemIey et al., 1980; Ishikawa et al., 2004; Ohmoto, 1996; Ohmoto and Takahashi, 1983; Singer and Kouda, 1988), which are also referred for the model interpretations.

The constructed models are then used to identify subseafloor hydrothermal fluid flow systems and accumulation mechanisms of major metal elements. This study is the first comprehensive application of the proposed geostatistical approach to modern SMS deposits to better understand the subseafloor distribution of metals.

2. Materials

2.1. Geologic setting

The Okinawa Trough is located in a back-arc basin, behind the Ryukyu Arc along the eastern margin of the Eurasian continent, which runs > 1200 km from Kyushu Island to Taiwan (Fig. 1a). The Okinawa Trough is regarded to be in the nascent stage of back-arc basin formation, namely, continental rifting prior to steady seafloor spreading, with an inferred extension rate of 23–46 mm/year (Hirata et al., 1991; Arai et al., 2017).

The Okinawa Trough is divided into northern, middle, and southern regions that are separated by the Tokara Strait and Kerama Gap at ~ 130°E and 127°E (e.g. Sibuet et al., 1987). The northern Okinawa Trough consists of several half-grabens covered by thick terrigenous material layers up to 8 km thick from the Yangtze and Yellow rivers in China, whereas the sedimentary cover ranges up to 2 km in the southern Okinawa Trough (Sibuet et al., 1987). The middle Okinawa Trough has received varying sedimentary supplies from those rivers, and their deposition rate has increased considerably over the past 0.5 Ma (Sibuet et al., 1987).

The Okinawa Trough is marked by volcanism with a bimodal basaltic-rhyolitic suite, accompanied by minor intermediate rocks (Ishikawa et al., 1991; Shinjo and Kato, 2000; Yamasaki, 2017, 2018). In the northern Ryukyu Arc, active volcanoes dominantly consist of andesitic rocks that define the volcanic front continuing from the Kyushu Island (e.g. Nakada, 1986; Shinjo and Kato, 2000). This volcanic front becomes unclear around the middle Okinawa Trough. The bimodal volcanic activity, which is typically associated with areas in rift zones (e.g. Martin and Piwinskii, 1972), in the middle Okinawa Trough is thus interpreted as transitional volcanism from arc to back-arc (Sibuet et al., 1987) or overlapping volcanism that occurred synchronously with that in the arc-trench system (e.g. Shinjo et al., 1999). The active volcanism results in vigorous seafloor hydrothermal activity in the middle Okinawa Trough (e.g. Glasby and Notsu, 2003). This activity formed sulfide/sulfate chimneys and mounds composed of sphalerite, galena, anhydrite, gypsum, and barite, as well as pyrite, chalcopyrite, marcasite, and/or tetrahedrite-tennantite with minor amounts of other minerals (Halbach et al., 1989, 1993; Nakashima et al., 1995; Ueno et al., 2003; Watanabe et al., 2006; Suzuki et al., 2008; Ishibashi et al., 2015; Nozaki et al., 2016, 2021a,b).

The study area, Izena Hole, is located in the middle Okinawa Trough and is a caldera-like seafloor depression in a rectangular shape of about 6 × 3 km with a maximum depth of 1660 m below sea level (mbsl) (Fig. 1b). Its floor is covered by up to 30 m of hemipelagic, unconsolidated silty clays (Ishibashi et al., 2015; Nozaki et al., 2018; Yamasaki, 2018). This depression is composed of unconsolidated sediments with sulfide-rich layers, tuff breccias, pumice exposed on the seafloor slopes, and a center cone-like small knoll of dacitic lava at the hole center formed by recent magmatic activity in which several normal faults trending E-W or ENE-WSW, parallel to the rifting axis of the middle Okinawa Trough, are distributed (Kato et al., 1989, 1990; Glasby and Notsu, 2003). There are two hydrothermal fields in this location: the JADE site (Halbach et al., 1989) in the northeast and the Hakurei Site (Maeda, et al., 1996; Morozumi et al., 2020) in the south accompanying active vents (or chimneys) (Fig. 1b) resulting from hydrothermal circulation on both large and small scales induced by a shallow heat flow source and controlled by faulting (Kinoshita and Yamano, 1997; Ishibashi et al., 2015). The Hakurei Site is known to be rich in Zn and Pb with polymetallic mineralization (Zn-Pb-Cu-Ag-Au with trace metal association) (Japan Oil, Gas and Metals National Corporation, 2013, 2016; Morozumi et al., 2020) of a kuroko-type VMS deposit. According to these references, the hydrothermal activity in the Hakurei Site extends over 500-m long from west to east, which is verified by a complex chimney structure with discharge of vigorous high-temperature fluids up to 326 °C in the vicinity of Dragon chimney (Ishibashi et al., 2014, 2015) (Fig. 1c).

2.2. Sample data for analysis

We chose a 700 × 200 m area (red box in Fig. 1b and 1c) in the Hakurei Site where six sites (I to VI) were drilled along approximately the E-W direction (Fig. 1c) with different depths of 72.5 m below seafloor (mbsf) (I), 46.5 mbsf (II), 180.0 mbsf (III), 120.5 mbsf (IV), 80.0 mbsf (V), and 80.5 mbsf (VI). Drill site I at the western edge was drilled from the top of a sulfide mound. A combination of the whole-rock geochemical compositions in the drilling core samples (ppm or wt.%) measured by ICP-QMS and lithological log data from onboard visual core descriptions were used for the spatial modeling. The target elements of ICP-QMS measurements for 454 samples were Na, Mg, Al, P, K, Ca, Sc, Ti, Mn, Fe, Co, Ni, Cu, Zn, Se, Rb, Sr, Y, Zr, Nb, Mo, Ag, Cd, In, Sn, Sb, Te, Cs, Ba, La, Ce, Pr, Nd, Sm, Eu, Gd, Tb, Dy, Ho, Er, Tm, Yb, Lu, Hf, Ta, W, Au, Tl, Pb, Bi, Th, and U. Sampling intervals along the drill hole depth direction ranged from 0.23 to 19.03 m with an average interval of 1.22 m. Intervals longer than 10 m were made owing to the poor core

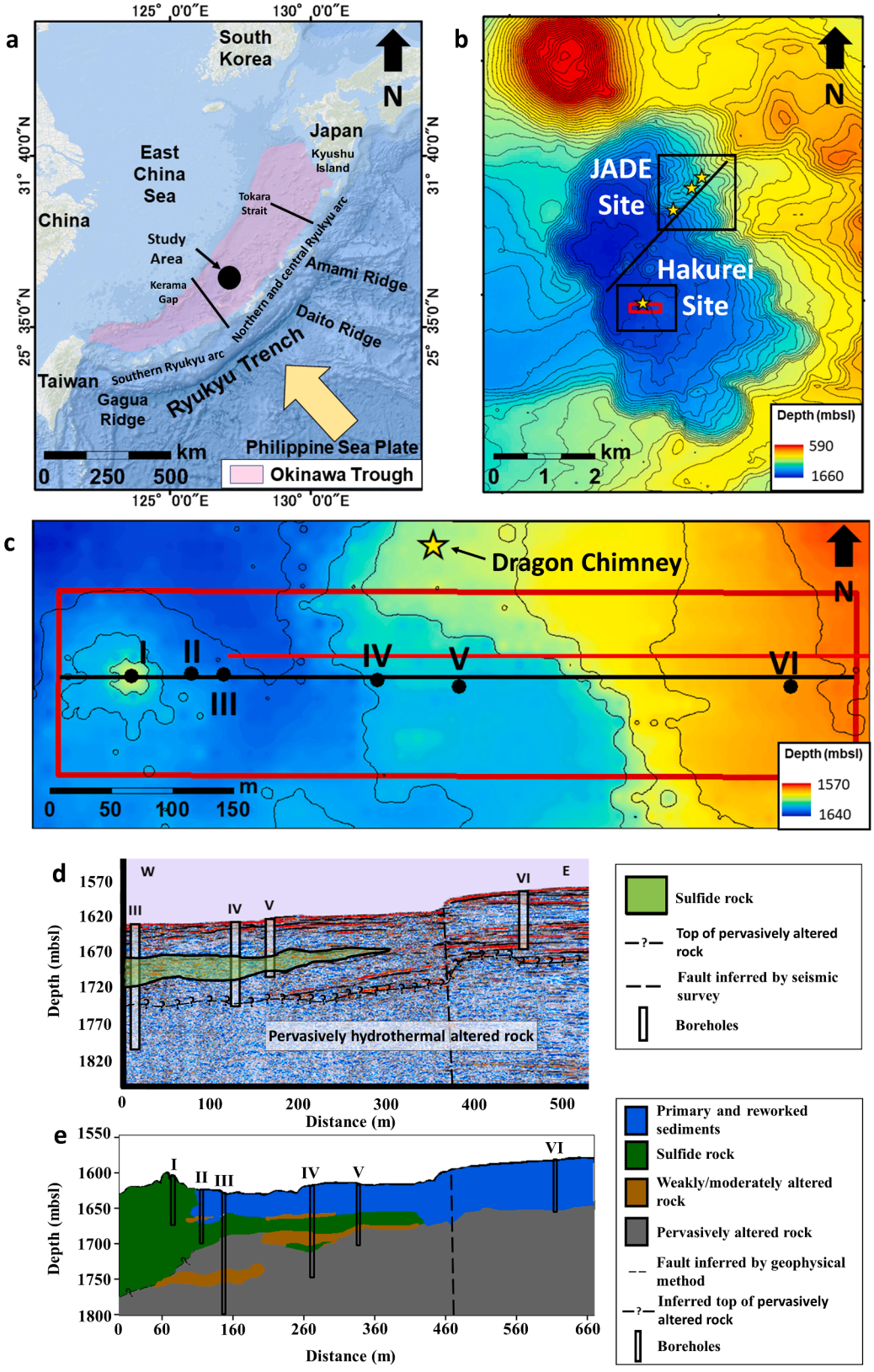

Fig. 1. Location of study area. (a) Tectonic setting of the Okinawa Trough in the East China Sea. (b) Topography of the Izena Hole with representative active hydrothermal vents marked by yellow stars with a distribution trend of large heat flow traced by a black line (Kinoshita and Yamano, 1997; Ishibashi et al., 2015). (c) Detailed topography of the study area with six drilling sites (I to VI) in which the red box represents the geostatistical modeling zone. (d) Seismic profile with interpretation of lithotypes and fault location (Asakawa et al., 2018). (e) Conceptual geologic model showing lithotype distribution produced from the drill hole lithotype data and the seismic profile. The locations of E-W seismic profile and conceptual geologic model are shown by red and black lines in (c), respectively.

recovery rate. When two samples were located within a short distance (10–20 cm) along a hole depth, the deeper sample was selected to unify lag distance of the semivariogram calculation. The two targeted samples have similar bulk geochemical compositions with elemental differences as small as 1%–2%. As a result, 454 samples were selected out of the original 462 samples.

On the basis of geologic descriptions for minerals, granulometrics, and texture characteristics, we classified and ultimately simplified the 247 geologic column data into four major lithotypes with common characteristics for geostatistical analyses: primary and reworked sediment, i.e. underwater debris flow deposit with pumiceous sediment (percentage of grouped samples out of the total samples: 43.3%), sulfide rock (29.2%), weakly/moderately altered rock (9.7%), and pervasively altered rock (17.8%). The definition of these lithotypes was based on the above-mentioned onboard visual core descriptions and X-ray diffraction analyses.

The first lithotype includes a mixture of hemipelagic sediment and various sizes of pumice blocks, turbidite, and laminated hemipelagic sediment with little or no hydrothermal alteration. Sulfide rock is dominated by sulfide minerals with barite and minor gangue minerals, weakly/moderately altered rock is composed of > 25% hydrothermally altered clay minerals, and pervasively altered rock is composed of > 90% of hydrothermally altered clay minerals. Weakly/moderately altered rocks and sulfide rocks are composed of primary minerals of quartz ± calcite ± albite with secondary montmorillonite ± illite ± chlorite ± K-feldspar ± dolomite ± kaolinite ± anhydrite ± pyrite and sphalerite + galena + barite + pyrite + marcasite ± chalcopyrite ± pyrrhotite ± cubanite, as determined from onboard X-ray diffraction analyses (Nozaki et al., 2018). Chalcopyrite is conspicuous in the samples from drill sites I and II and becomes progressively rare toward the eastern drill site V. Pyrite is present in both lithotypes but less abundant in the weakly/moderately altered rocks.

2.3. General geological structure

Geologic structures below the seafloor are inferred from seismic profiles obtained from reflection surveys in an area covering four drill sites (III to VI) (Fig. 1d). This profile outlines a stratiform layer with a high-velocity anomaly that likely hosts sulfide rocks and weakly/moderately altered rock. These stratified zones are regarded to be strongly deformed and act as pathways for hydrothermal fluids (Asakawa et al., 2018). Another important structure observed from the seismic profile is the development of a fault between drill sites V and VI in the deepest part to the seafloor.

A conceptual geologic model is produced using the seismic profile survey and drill site lithotype (Fig. 1e) by referring to previous models in a similar geologic setting in the Okinawa Trough (Glasby and Notsu, 2003; Ishibashi et al., 2014, 2015). Apart from the westmost sulfide mound, the top layer consists of primary and reworked sediments with variable sizes of pumice fragments by a mixing of underwater debris flows from the surrounding slopes and hemipelagic sediments (Nozaki et al., 2018; Yamasaki, 2018).

3. Methods

The methods in this study consists of pre-processing of the content data using the centered log-ratio (clr) transformation, statistical methods using PCA to decrease the dimensionality of the content data and k-means clustering to classify content data into several groups with similar mineral assemblage trends, and two geostatistical and conditional simulations, turning bands simulation (TBSIM) and pluri-Gaussian simulation (PGSIM), to implement spatial modeling of geochemical composition and categorical data (either lithotypes or cluster numbers generated by k-means method), respectively. The flow of total analyses using these methods is summarized in a flowchart (Fig. 2).

3.1. Data pre-processing

The content data of various elements are regarded as multivariate dataset. Because the content ranges are largely element-sensitive, appropriate data pre-processing is necessary to standardize each value. Special caution is required for standardization because incorrect methods can distort covariance, which changes the actual strengths of relationships between variables (Davis, 2012). The covariance matrix is essential in PCA. As a standardization method, we adopt the clr transformation that can remove spurious negative correlations between compositional variables (Aitchison and Greenacre, 2002), although such negative correlations are generally an issue for major elements such as Si, Al, and Ca, which are not used in this study. In this method, the

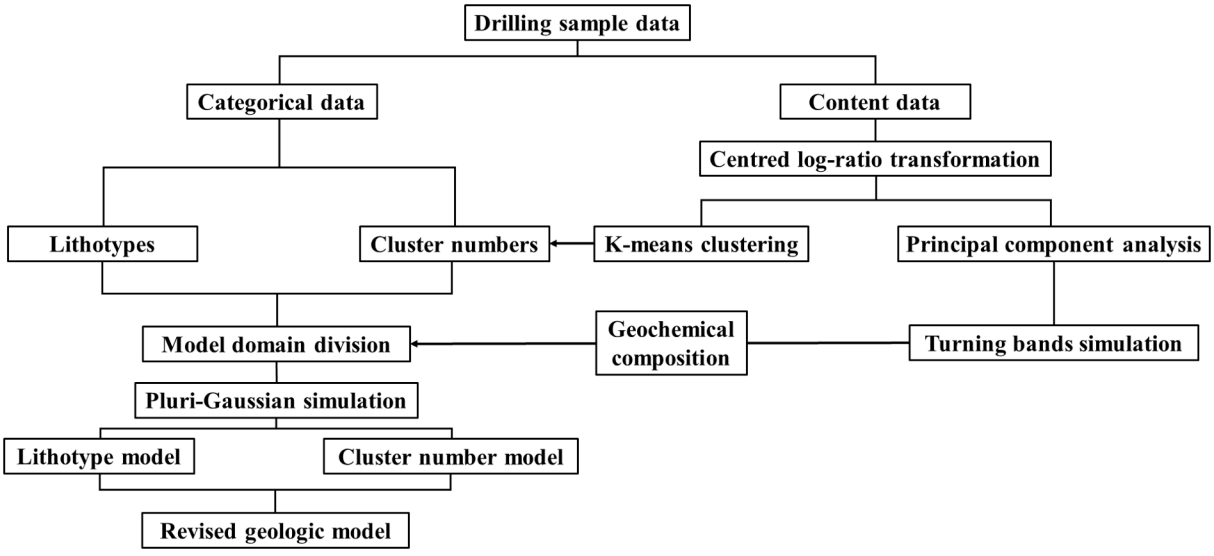

Fig. 2. Flowchart showing flows of data analyses composed of pre-processing of the content data using the centered log-ratio transformation, statistical methods using PCA to decrease the dimensionality of the content data and k-means clustering to classify content data into several groups with similar mineral assemblage trends, and geostatistical spatial modeling using turning bands simulation for geochemical composition and pluri-Gaussian simulation for categorical data (either lithotypes or cluster numbers generated by k-means method).

content data of a certain element from a sample, x_i, is transformed into log data using the geometric mean (g_D) according to:

$$\mathrm{clr}(x_i) = \ln \frac{x_i}{g_D(x)} \quad (1)$$

$$g_D = \left(\prod_{j=1}^{m} x_j \right)^{1/m} = \sqrt[m]{x_1 . \; x_2 \ldots x_m} \quad (2)$$

where m is the number of elements. The suitability of clr transformations to derive a reliable covariance matrix for PCA has been demonstrated in several previous case studies (e.g. Aitchison, 2002a, 2002b; Pawlowsky-Glahn and Olea, 2004; Carranza, 2011; Pawlowsky-Glahn et al., 2015).

3.2. Statistical methods

The clr-transformed data are then used for PCA and clustering. PCA has been widely applied to distinguish geochemical anomalies in exploratory data (e.g. Dempster et al., 2013; Shahi, 2017). The dimensionality of the content data is decreased by linearly combining elements with similar variances and chemical similarities, which may contribute to the identification of highly mineralized zones. The new variable generated by the linear combination is termed principal component (PC).

K-means clustering aims to classify content data by examining the dependence of geochemical compositions on lithotype. Its effectiveness has been demonstrated in several previous case studies (e.g. Iwamori et al., 2017; Zhou et al., 2018). This method is expected to supplement the subjective and qualitative geological interpretations and assist in the consideration of content characteristics by correlating elemental concentrations with lithotype.

3.3. Geostatistical methods

TBSIM overcomes drawbacks of the simulation method that sequentially draws a value at each simulation point from a conditional distribution given by the previously simulated data and values (Chilès and Delfiner, 2012). Although the sequential method has been used widely in geologic, hydrogeologic, and environment applications to characterize unsampled values of regionalized attributes (Emery and Lantuéjoul, 2006), it may produce a biased result by error propagation with the use of moving neighborhood data for successive conditional simulations. On the contrary, the non-conditional simulation step in TBSIM can reduce such errors, and all realizations can be converted into conditional data by a kriging calculation.

In addition, PGSIM based on the truncated Gaussian method (Matheron et al., 1987) is known to be well suited for simulating geological configurations by organizing lithotypes into sedimentary sequences and vertical and horizontal interfingering relationships (Armstrong et al., 2011; Delfiner and Chilès, 2012). PGSIM is achieved by simulating two or more Gaussian variables at every point in the domain and honoring the lithotype rule regarding the proportions and contact among the lithotypes and by converting the variables into lithotypes (Armstrong et al., 2011; Delfiner and Chilès, 2012). PGSIM can reproduce a lithotype ordering relationship by conditioning both the semivariograms and vertical proportion of each lithotype (Armstrong et al., 2011; Pyrcz and Deutsch, 2014). The resultant geologic modeling is therefore more realistic than a straightforward semivariogram-based simulation of categorical variable modeling, typically sequential indicator simulation (Journel, 1983; Journel and Alabert, 1988; Deutsch and Journel, 1998), which constrains only the spatial continuity of each category.

For both models, the study area was gridded by voxels of a unit size of 10 m along the *X*-axis (E-W), 10 m along the *Y*-axis (N-S), and 0.4 m along the *Z*-axis (depth direction). The horizontal size was set to consider the nugget effect and data range of the semivariograms. The vertical size was determined by considering the average interval of neighboring sampling points along the drill sites to capture subtle changes in content or lithotype. The bottom location of the longest drill site (III) was used as the bottom boundary of the modeling domain. Because the lithotype data of drill site VI were mostly homogenous except for the deepest core, PGSIM was targeted from the western edge to the fault location (Fig. 1d).

3.3.1. Turning bands simulation (TBSIM)

TBSIM was implemented to delimit highly mineralized zones with high metal contents using the PC values. The TBSIM principle and algorithm are described in detail in several references (Olea, 1999; Emery and Lantuéjoul, 2006; Chilès and Delfiner, 2012). Unlike common covariance-based direct simulations in $\mathbb{R}^n$, TBSIM is basically a 1D simulation on a line, which requires two steps: (i) unconditional simulation using spatial covariance function of the data on a line and (ii) conditioning correction to connect the simulated value at a data location with the data value by simple kriging. Let kriged values at location $\mathbf{u}$ using the sample data and unconditional simulated data be $y^*_{kc}(\mathbf{u})$ and $y^*_{ku}(\mathbf{u})$, respectively. The conditional realization $y^l_{CS}(\mathbf{u})$ is formulated using the unconditional realization $y^l_{uc}(\mathbf{u})$and following equation (Pyrcz and Deutsch, 2014):

$$y^l_{CS}(\boldsymbol{u}) = y^l_{uc}(\boldsymbol{u}) + \left\{ y^*_{kc}(\boldsymbol{u}) - y^*_{ku}(\boldsymbol{u}) \right\} \quad (3)$$

TBSIM performance depends on the number of lines and how to simulate one-dimensional random field at the first step (Paravarzar et al., 2015). Although TBSIM can reproduce the covariance model without bias regardless of the number of lines, hundreds of lines at each voxel are recommended for three-dimensional modeling (Emery and Lantuéjoul, 2006). We then set 1000 lines and executed only one realization on each line. The TBSIM result is shown as an e-type model by averaging 100 realizations.

3.3.2. Pluri-Gaussian simulation (PGSIM)

PGSIM has been used for categorical and non-numerical data, such as lithotype. The spatial models of lithotype and cluster number by k-means were produced by PGSIM. Fig. 3 schematically illustrates the following five steps.

(I) Data input: a categorical variable (lithotype or cluster number) i_k takes a value of 1 if the category k is present or 0 otherwise.

(II) Production of vertical proportions curves: vertical proportions are computed along lines parallel to a chosen reference level, which is generally a chrono-stratigraphic marker. We chose the sulfide rock layer as the main level owing to its significant presence. The proportion curves tend to vary laterally and vertically in a study domain. Such non-stationary phenomena originate from geologic heterogeneity-fluctuating semivariograms. Use of a 3D matrix of proportion curves can smooth the fluctuation, as demonstrated in detail in Armstrong et al. (2011).

(III) Definition of the lithotype rule and semivariogram fitting: the lithotype rule is a diagram that defines contact relationships at the boundary of different lithotypes. When the indicator variables are in contact with the lithotype rule diagram, the corresponding variables are connected in the simulation. The transitions of the indicator variables follow the transition statistics composed of two probability matrices (downward and upward) showing the vertical downward and upward transition frequencies between indicator variables along drill sites (Armstrong et al., 2011). In addition, two Gaussian random functions, G1 (horizontal axis) and G2 (vertical axis), independent of one another are generated and truncated to yield four categorical variables for the case shown in Fig. 3. The area of each lithotype in G1 and G2 is equal to its proportion (Delfiner and Chilès, 2012). The semivariogram models of G1 and G2 are determined by repeatedly changing the

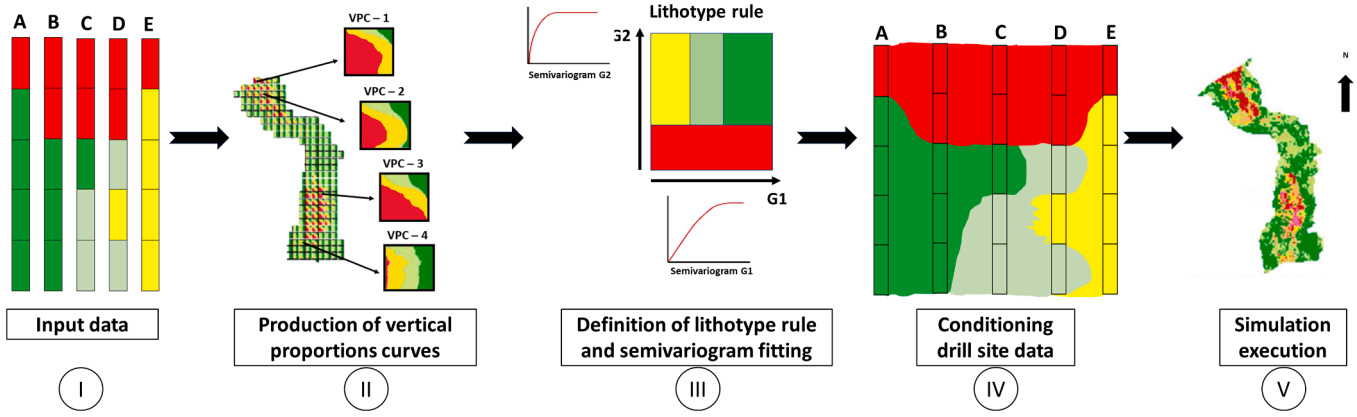

Fig. 3. Schematic workflow of a pluri-Gaussian simulation with an example of four lithotypes from Armstrong et al. (2011). G1 and G2 represent two Gaussian random functions.

ranges as follows. An unconditional pluri-Gaussian simulation is first executed by defining the type and parameters of the semivariogram models. A least-square gradient-based minimization algorithm is then used to update the semivariogram models so that they match with the experimental semivariograms (Mariethoz et al., 2009).

(IV) Conditioning drill site data: A Gibbs sampler algorithm was used to iteratively re-simulate the Gaussian fields for reconstructing both the semivariograms model and constraints (Armstrong et al., 2011; Chilès and Delfiner, 2012).

(V) Simulation execution: TBSIM was used to simulate each Gaussian variable. The simulation result must reproduce the main features contained in the drill site data, semivariograms, and proportions of each lithotype.

As easily inferable, the one lithotype rule is insufficient to simulate complicated formation structures. The study domain was then divided into subzones on the basis of the TBSIM results. PGSIM was individually applied to each subzone unit and their results merged.

4. Results and discussion

The following results were obtained using the clr-transformed content data, expressed, for example, as Zn* for the original data Zn.

4.1. Data selection and grouping of metals by principal component analysis

Because many elements (52) were measured for the bulk-rock geochemical compositions, we first selected elements that were essential for characterizing a SMS deposit using a loading plot (Fig. 4a). The horizontal and vertical axes of this circle show that PC1 and PC2 respectively highlight significant elements that are correlated with one another by the (i) line length from the circle center and (ii) angle between two lines of an element pair. The elements with longer line lengths are more essential because of their large loadings. The elements contained within highly mineralized zones, generally include Zn*, Pb*, Cu*, Ba*, Cd*, and Ag*, and were observed to have large PC1 loadings. The by-product elements of hydrothermal activity, Sn* and Mn*, show low PC1 loadings and large PC2 loadings. Significant positive correlations between a pair are identified by small angles, no correlation by right angles, and significant negative correlation by point symmetry (i.e. two elements are located on opposite sides). Eight elements, Zn*, Pb*, Cu*, Ag*, Ba*, Cd*, Mn*, and Sn*, were selected as highly correlated variables and used for the subsequent PCA analysis. Among them, base metals Zn*, Pb*, and Cu* are the most strongly correlated because their

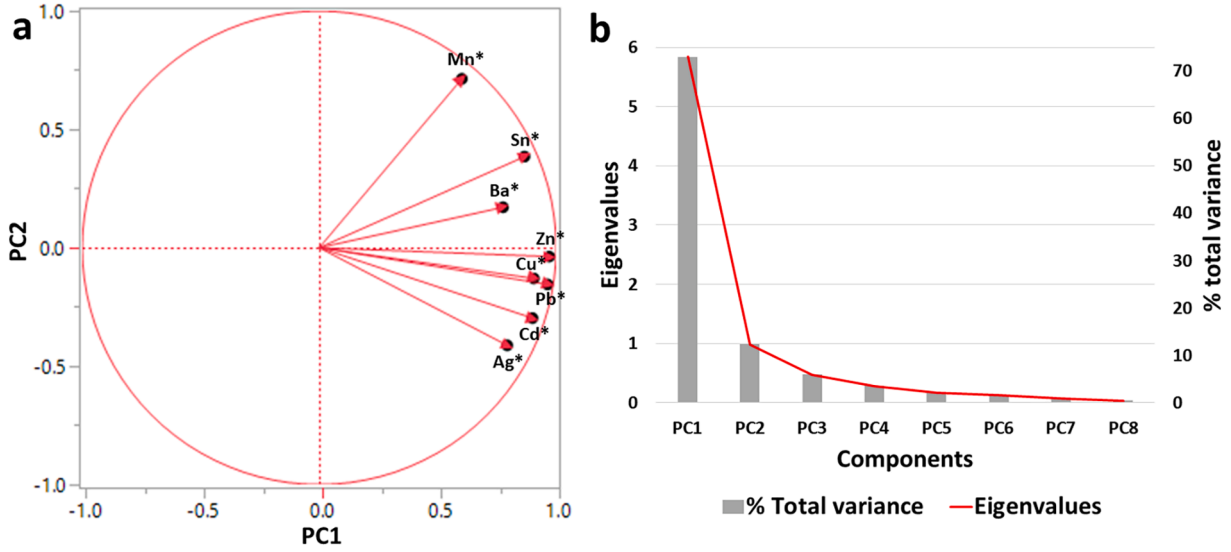

Fig. 4. (a) Loading plot showing elemental correlations of centered log-ratio transformed content data. Only correlated elements are displayed. PC1 and PC2 denote the two first principal components (PCs). (b) Eigenvalues of PCs (lines) and percentage of each eigenvalue to the total variance (bars).

two-pair angles are substantially smaller than the other pair angles.

The eigenvalues and contributions to the total variance of each PC (PC1–PC8) are shown in a scree diagram (Fig. 4b), which shows that most information is retained in PC1 by its particularly large variance (73.0%). PC2′s variance is 12.3% and the sum of the variances from PC3 to PC8 is as small as 14.7%. Therefore, only PC1 and PC2 were selected for TBSIM to locate high-metal-content zones and interpret the sulfide/sulfate mineralization process.

4.2. Characterization of metal assemblage by clustering

The eight elements were classified into four clusters by k-means because this number of groups was the most suitable to discriminate the difference in metal assemblages among the clusters, as shown by a biplot of PC1 and PC2 (Fig. 5a). The differences of clusters are characterized by the difference in signs of PC1 and PC2. For example, the signs of PC1 and PC2 are generally in clusters 1 (-, +), 2 (-, -), 3 (+, +), and 4 (+, +), and the difference in PC1 values are located the farthest in clusters 2 and 3. Cluster 1 is the most representative, including 75% of the 454 samples, whereas cluster 2 is the smallest with only 3% (Fig. 5b). With regards to the relationship between lithotype and cluster (Fig. 5c), lithotype mixtures appear in clusters 1 and 2, which may be because these clusters are mainly distributed in the absence of hydrothermal activity or weak alteration by hydrothermal fluids, as discussed later. In contrast, clusters 3 and 4 are mostly dominated by sulfide rock and weakly/moderately altered rock, respectively.

Differences between the eight elemental contents are revealed by their median values in each lithotype (Fig. 6a, 6b) and cluster (Fig. 6c, 6d) by dividing the elements into two groups depending on their content magnitude. Sulfide rock and clusters 3 and 4 show a similar pattern such that seven elements (except for Mn) are higher than in the other lithotypes and clusters. Clusters 3 and 4 can be a target of metal resources because of particularly higher base metal contents, especially cluster 3 by its abundant Zn. They are distinguished by differences in Ba and Mn contents: Ba is scarce in cluster 3. The other lithotypes, primary and reworked sediments, weakly/moderately altered rock, and pervasively altered rock are similar in their low Zn, Pb, Cu, Ag, Sn, and Cd contents and are distinguished by differences in Ba and Mn. Pervasively altered rock is characterized by the highest Ba and Mn contents. Clusters 1 and 2 also low contents for the seven elements except for Mn. Considering Mn occurrences in the uppermost layer, the presence of Mn hydroxides derived from hydrothermal plume (e.g. German et al., 1990, 1991) is inferred to be widespread on the seafloor.

4.3. Metal-content distribution by TBSIM

Because most features are summarized in PC1, this group was targeted for spatial modeling by TBSIM. Following the principle of geostatistics, the PC1 values preferably follow a normal distribution. However, PC1 values show a strong positive skewness (Fig. 7a), which means that the clr transformation did not adequately remove the effect of trace elements with small variance on the correlations between elements. To obtain a desirable Gaussian distribution of the PC1 values, the normal score transformation was applied to the PC1 values to transform them into a normal standard distribution with 0 mean and 1.0 variance (Fig. 7b). This transformation preserves the ordering and spatial relationships of the data. The simulated results were then linearly back-transformed into the original data scale.

The spatial correlation structure of the transformed data was quantified by semivariograms along two directions: the omnidirectional horizontal direction in the *XY* plane and vertical direction of the *Z* axis. Both experimental semivariograms are well fitted to the spherical model, as shown by the curves in Fig. 7c. The ranges are defined as 120 and 90 m along the horizontal and vertical directions, respectively, from the spherical model.

Accuracy of the geostatistical modeling was checked by a cross-validation procedure that uses a scatterplot between the true (ordinate) and predicted values (abscissa) at data locations from neighboring data (Fig. 7d). Ordinary kriging was adopted for cross-validation to check the suitability of the semivariogram models and neighborhood search setting using an ellipse or circle. Considering the ranges, the search area was set to an ellipse with 120 m along the *XY* plane and 90 m along the *Z* axis. The correlation between the true and predicted values is relatively high (linear correlation coefficient $\rho = 0.79$), which verifies the suitability and feasibility of TBSIM using the models and search setting. The scatterplot shows also larger overestimates and

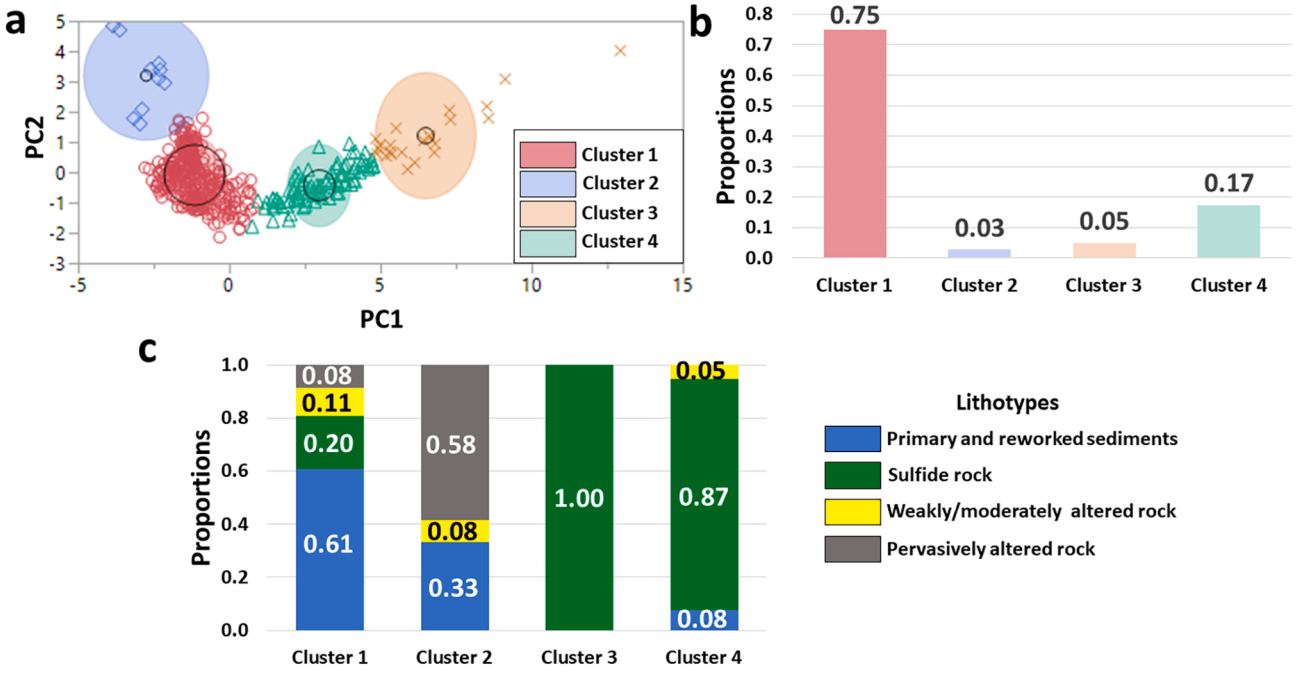

Fig. 5. Results of k-means cluster analysis for eight correlated elements: (a) biplot of PC1 and PC2 showing cluster features; (b) ratio of sample number classified into four clusters and; (c) stacked bar chart depicting occurrence ratio of four lithotypes in each cluster.

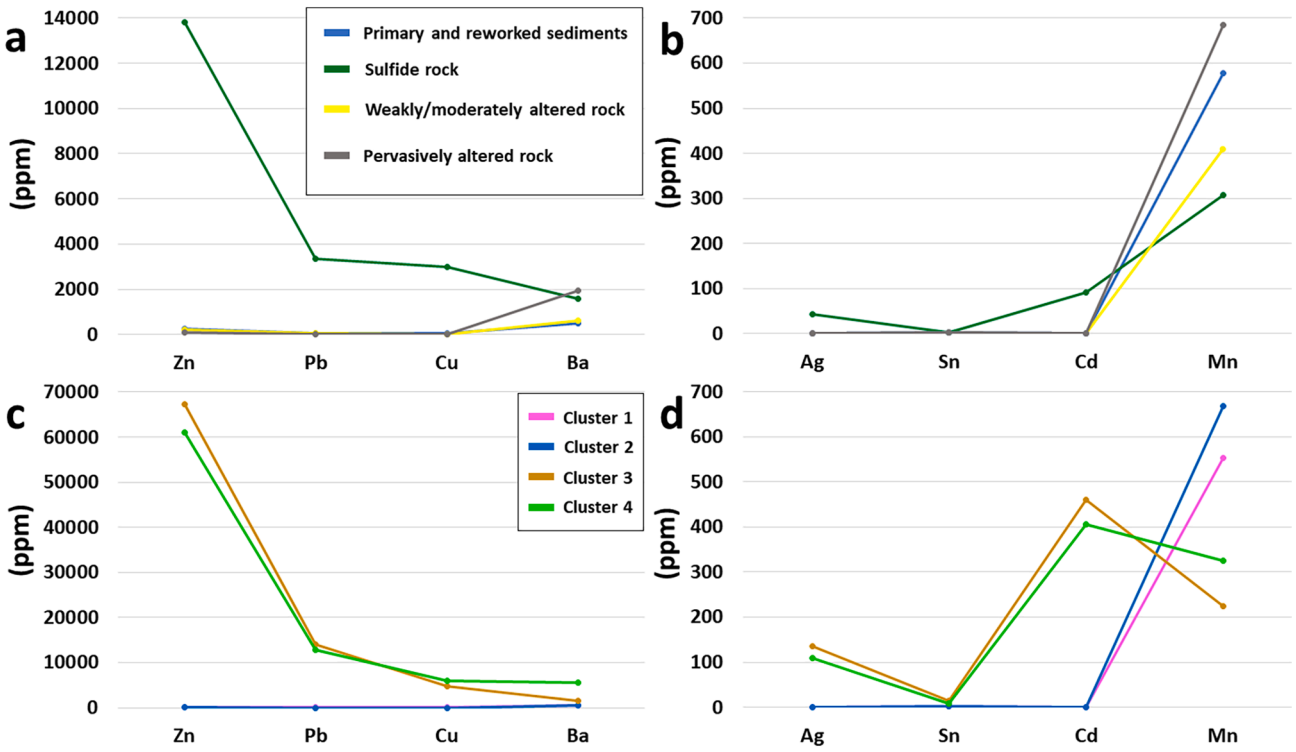

Fig. 6. Median contents of eight elements used for PCA in each lithotype (a and b) and cluster (c and d). Clusters 1 and 2 overlap in (c) and (d) except for Mn.

underestimates of the PC values close to the minimum and maximum, respectively (Fig. 7d). This decrease in the accuracy is mainly caused by the too sparse distribution of sample data in the deep region as shown in Fig. 1e. However, the predicted values are fallen within a certain range around the 45° line except for particularly distant several data. The accuracy of TBSIM was also demonstrated by our previous study (de Sá et al., 2020).

The e-type TBSIM results are shown by PC1 distributions on the seafloor and at an E-W cross-section that passes the drill site locations (Fig. 8a, 8b). High PC1 values are clearly concentrated on the western side of the active vent near drill site I and also in the western side of the inferred fault. An E-W vertical cross-section with *iso*-planes of the PC1 values reveals that high values greater than PC1 = 4.0 are thickly distributed underneath the sulfide mound, suggesting stockwork formation (Fig. 8b). In addition, horizontal/stratiform mineralization seems to occur from the mound toward the east until the inferred fault, as shown by the elongated zone enclosed by the *iso*-plane of PC1 = 4.0. Highly permeable pumiceous and sedimentary materials are thought to be distributed in the mineralized zone where diffusive flows may percolate through the pores.

Low values less than PC1 = 2.0 around drill site VI imply the absence of hydrothermal activity in the western side of the fault. By tracing the zones with PC1 > 4.0 from 1800 mbsl to the seafloor in the western fault, the fault may have acted as a barrier for hydrothermal flows from the west and transported them along it.

Considering the stratiform mineralization and effects of hydrothermal activity from the western boundary to the inferred fault, this subarea was divided into three zones following the *iso*-plane of PC1 = 4.0 for PGSIM (Fig. 8c). The top zone (A) is mainly unrelated to hydrothermal alteration and composed of primary and reworked sediments. The middle zone (B) is a major mineralization zone containing the massive sulfide mound, stockwork, and horizontal/stratiform subseafloor sulfide layer. The bottom zone (C) mainly consists of pervasively altered rock. These results reveal a discontinuous geologic distribution induced by the inferred fault and require that the model domain be resized to optimize the PGSIM application by considering the fault location. The easternmost limit was rearranged to suit the distal edge of the polymetallic sulfide body, shortening the E-W length from 700 to 500 m, while the vertical range remained unaltered.

4.4. Lithotype modeling by PGSIM

The lithotype rules and indicator semivariograms of the lithotypes and cluster numbers along the omnidirectional horizontal and vertical directions were separately produced for zones A, B, and C, as shown in Fig. 9 (lithotypes) and Fig. 10 (cluster numbers). The area of each rectangle in a lithotype rule is proportional to the frequency of each lithotype or cluster number (i.e., number of data points out of the total number). In all three zones, the ranges of horizontal and vertical semivariograms were approximated as 70 and 15 m, respectively. The experimental semivariograms were fitted to an exponential model for zone B and a Gaussian covariance model for zones A and C. The fitting degree of the horizontal experimental semivariograms to the models was worse than that of the vertical experimental semivariograms for the lithotype because their rock horizontal distributions were more heterogeneous, and the number of drill site locations is particularly limited. Reliability of the experimental semivariograms depends on the number of sampled data. The model fitting was therefore better for the cluster number along both the directions because more data are available.

The lithotype rules and two sets of conditioning data (except for drill site VI) were used for 215 and 363 of the lithotype and cluster number simulations, respectively. The results are shown by the seafloor distributions (Fig. 11a, b), perspective view from the southeast (Fig. 11c, d), and an E-W cross-section (Fig. 11e, f) of the same location as Fig. 8b. On the seafloor, the mineralization-related lithotype, sulfide rock, and high-metal-content clusters 3 and 4 are concentrated around the sulfide mound similar to the TBSIM result of PC1, whereas the primary and reworked sediments and cluster 1 without evidence of hydrothermal alteration are predominantly distributed on the eastern side. Fig. 11c and d show the distributions of lithotypes and cluster numbers, and highlight the concentration of hydrothermal activity and mineralization occurrences in zone B.

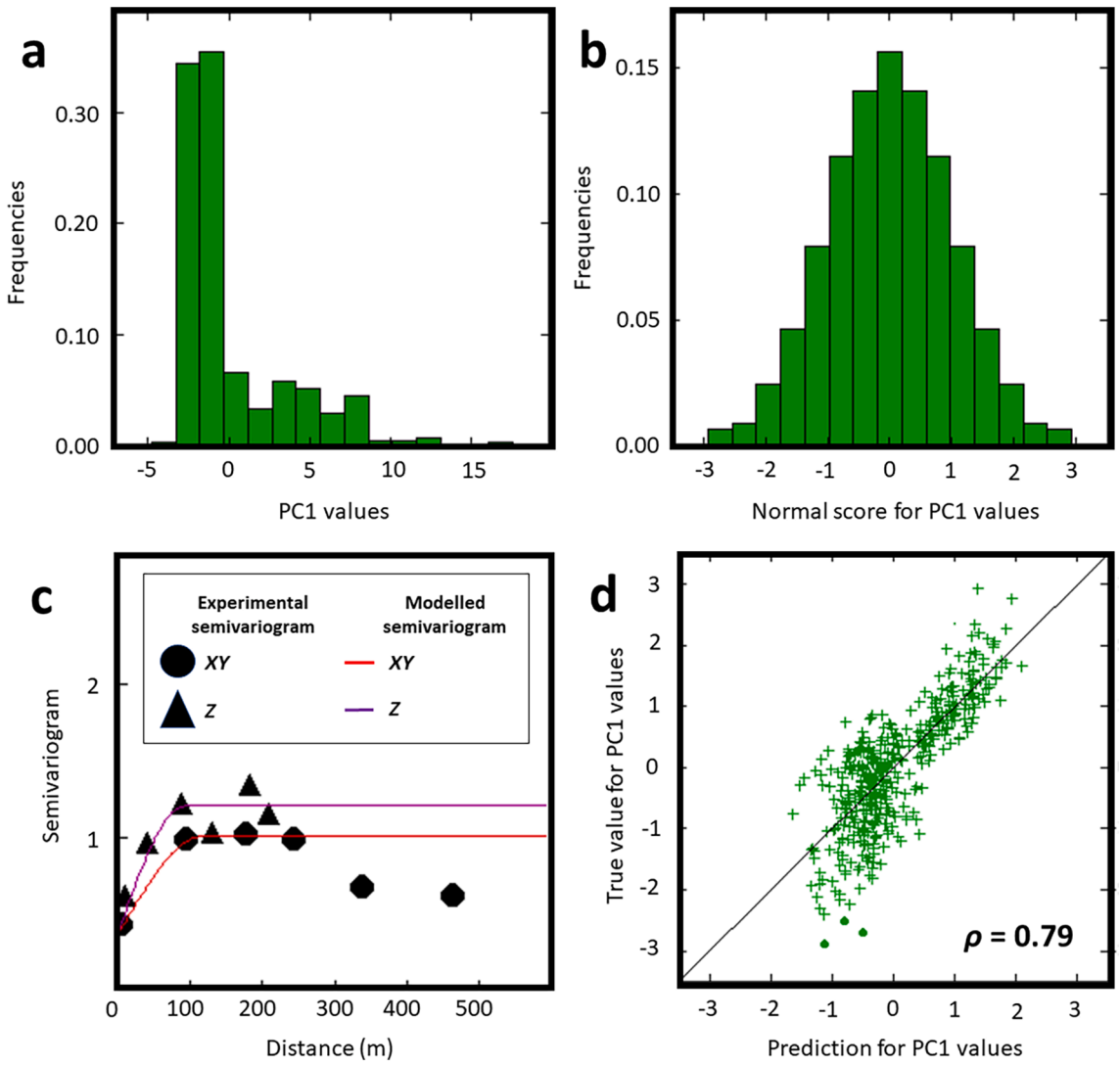

Fig. 7. Results of geostatistical analysis. Histograms of (a) original PC1 values and (b) normal score transformed values. (c) Experimental and modeled semivariograms (represented by diamonds and curves, respectively) of the transformed dataset along two directions: the omnidirectional horizontal direction (red curve) and vertical direction (purple curve). (d) Cross-plot between the true and predicted PC1 normal scores by ordinary kriging, showing the kriging calculating accuracy and suitability of the semivariogram models and neighborhood data searching setting. A spherical model was used for the fitting.

Characteristics of the lithotype and cluster number distributions are revealed more clearly by the cross-section, which confirms that the lithotype model is well fitted to the conceptual geologic model (Fig. 1e) and supports the suitability of the zone divisions, lithotype rule, and semivariogram models. A remarkable feature includes the geologic significance of cluster 4 in mineralized zone B as a halo of high-metal-content cluster 3 because it is thinly distributed along the edges of the sulfide rock lithotype. The most plausible explanation of this halo is hydrothermal alteration along the flow paths. The distribution of cluster 1 overlaps with lithotypes of unrelated hydrothermal activity, primary and reworked sediments, and pervasively altered rock in zones A and C. The distribution of cluster 2 in zone C overlaps with weakly/moderately altered rock. Although cluster 2 is low in metal contents (Fig. 5a), the weakly/moderately altered rock in zone C contains chlorite group minerals in drill site III and hydrothermal clay with a pyrrhotite + (iso) cubanite vein in drill site IV. Such mineral characteristics suggest the formation of hydrothermal flow pathways in zone C along which mineralization scarcely occurred.

4.5. *Improvement of lithotype model for interpretation of the hydrothermal flow system*

By integrating the lithotypes in each cluster number (Fig. 5c) and PGSIM results of lithotype and cluster number, relationships of lithotype with cluster number and features of polymetallic contents in each cluster detected from the PCA analysis (Fig. 6) can be identified, as summarized in Table 1. Cluster 1 covers two lithotypes, primary and reworked sediments and pervasively altered rock, and is poor in polymetallic contents except for Mn. In the top zone, the presence of Mn is related to discharge of the hydrothermal fluids from chimneys (i.e., hydrothermal plumes) and commonly found in turbiditic and hemipelagic sediments as forms of Fe-Mn hydroxide and oxide (e.g. German et al., 1990, 1991). Seawater provides an oxidization environment for Mn precipitation above sulfide zones as well as in areas distal from the vents. Sulfide rock was assigned to cluster 3, which is mostly contained in zone B and a highly mineralized zone. This zone also includes cluster 4 whose composition is similar to that of cluster 3 with slightly higher Ba and Mn contents owing to the occurrence of sulfate minerals. Weakly/moderately altered rock lithotypes are separated into two clusters: cluster 4 with mineralized features rich in polymetallic elements and cluster 2,

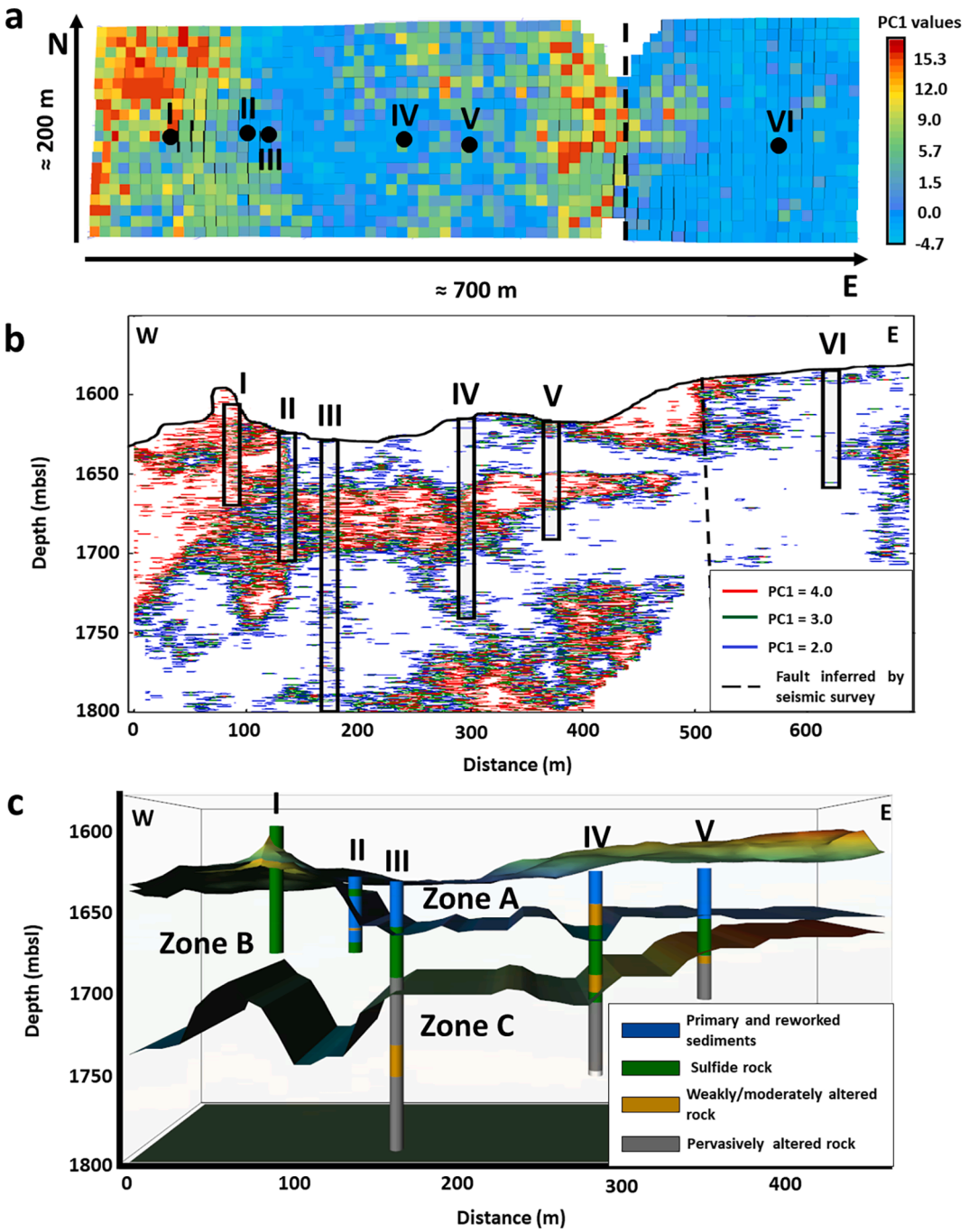

Fig. 8. PC1 value distribution by TBSIM on the seafloor (a), (b) at an E-W vertical cross-section along the line in Fig. 1c, (c) a perspective view of the *iso*-surface of PC1 = 4.0 of the three zones divided for lithotype simulations by PGSIM, and geologic columns. The TBSIM result is an e-type model by averaging 100 realizations.

which is poor in these features and forms strings in zone C. Simplified lithologic properties are merged into the onboard visual core descriptions listed in Table 1.

Using the relationship between lithotype and cluster number (Table 1), the PGSIM results of cluster numbers (Fig. 11) were transformed into lithotype: cluster 1 to primary and reworked sediments in the shallow part and pervasively altered rock in the deep part; cluster 2 to weakly/moderately altered rock; cluster 3 to sulfide rock; and cluster 4 to weakly/moderately altered rock. The purpose of this transformation was to improve the PGSIM geologic model on the basis of subjective drilling core observations.

Fig. 12 is a resulting revised geologic model along an E-W cross-section with the same locations of Fig. 8b, 11e, and f. This improved model can provide a more detailed delineation of the distributions of sulfide rock and stockwork underneath drill site I, which is located near the sulfide mound with a chimney, as well as small discontinuous distributions of sulfide rock between drill sites II and V in the zone of hydrothermally altered rock. The distribution of sulfide rock in Fig. 12 suggests two fluid flows with high probability (red arrows). The ascent flows toward the sulfide mound and the lateral flows from the stockwork zone toward its adjacent permeable layers. The former flow may be predominant because mineralization is concentrated on the seafloor and in the shallow subseafloor. The latter flow induces large heat loss without forming a chimney or mound and causes horizontal/stratiform alteration and mineralization (i.e. replacement alteration/mineralization) (Doyle and Allen, 2003; Tornos et al., 2015). Such subseafloor

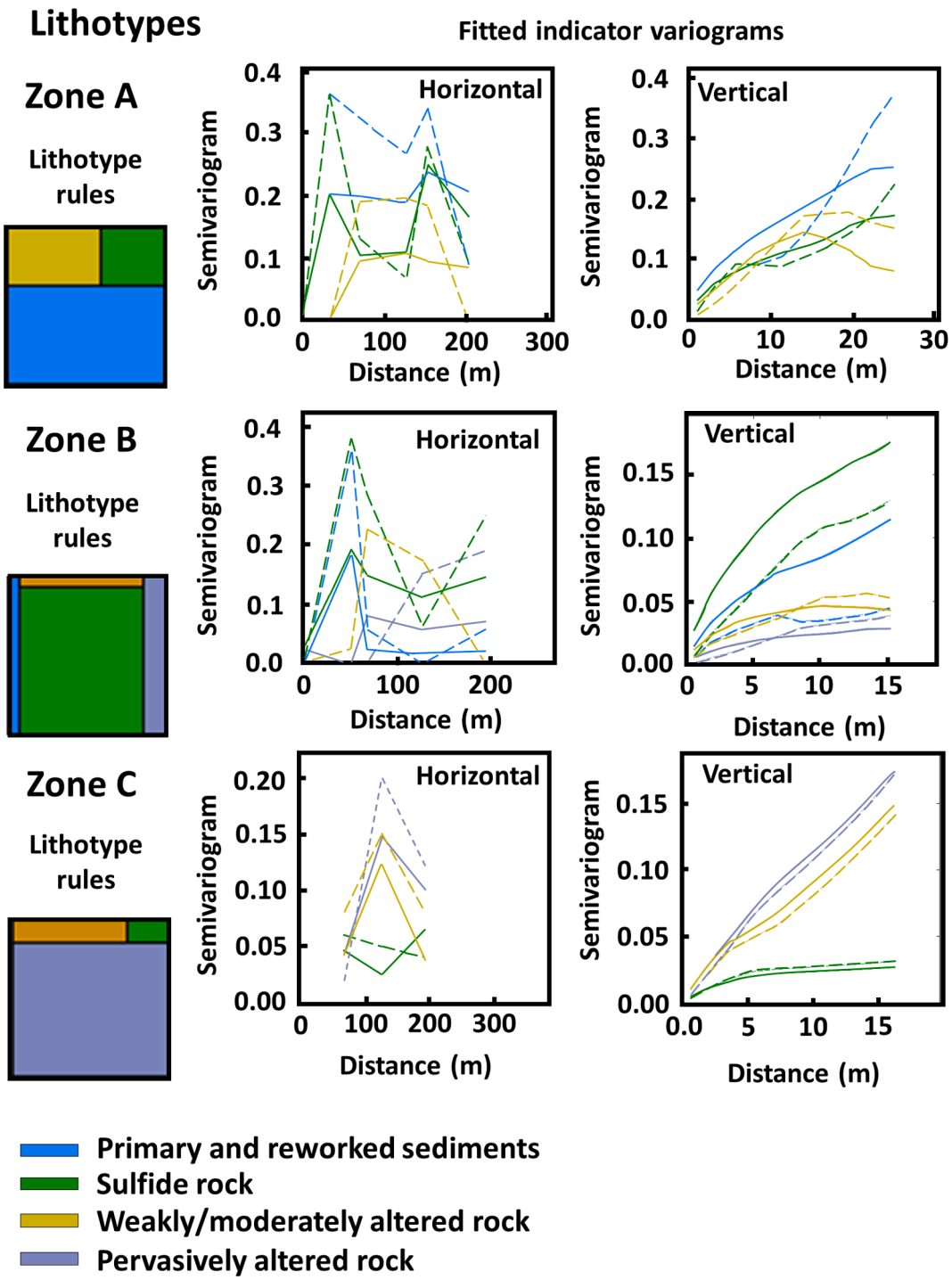

Fig. 9. Lithotype rule diagrams and indicator variograms along the omnidirectional horizontal and vertical directions of the four lithotypes in the three zones shown in Fig. 7c. The dashed and solid lines denote the experimental and modeled semivariograms, respectively.

replacement mineralization is consistent with the different Pb and S isotope signatures between the mound sulfide and subseafloor sulfide body (Totsuka et al., 2019; Nozaki et al., 2021a).

In addition to the numerous studies regarding kuroko deposits in Japan, analogue VMS deposits on land are also helpful to understand the transport and precipitation mechanism of polymetallic metals in hydrothermal systems in the Okinawa Trough. In shallow portions of active hydrothermal systems in the seafloor, such as in the Hakurei Site, the main factors that control the mineral assemblage stability are temperature, pH, and pressure (Robb, 2004). Similar to the kuroko deposits, the main minerals in this study area are sphalerite, galena, barite, and pyrite (Ishikawa et al., 2004; Ishibashi et al., 2015; Nozaki et al., 2016), which are considered to have precipitated by mixing of cold seawater with hot hydrothermal fluids in a temperature range from approximately 200 to 300 °C (Herzig and Hannington, 1995). Cu-rich minerals, typically chalcopyrite, precipitated in the inner and lower parts of the stockwork near the chimney in a higher temperature range from 280 to 380 °C (Sato, 1974; Date et al., 1983; Eldridge et al., 1983; Ohmoto and Takahashi, 1983; Ohmoto, 1996). Portions of sphalerite and galena grains can be dissolved and remobilized to the shallower part during zone-refining when hot hydrothermal fluid returns into the system (e.g. Ohmoto, 1996). The appearance of a kuroko-like zoning pattern in the

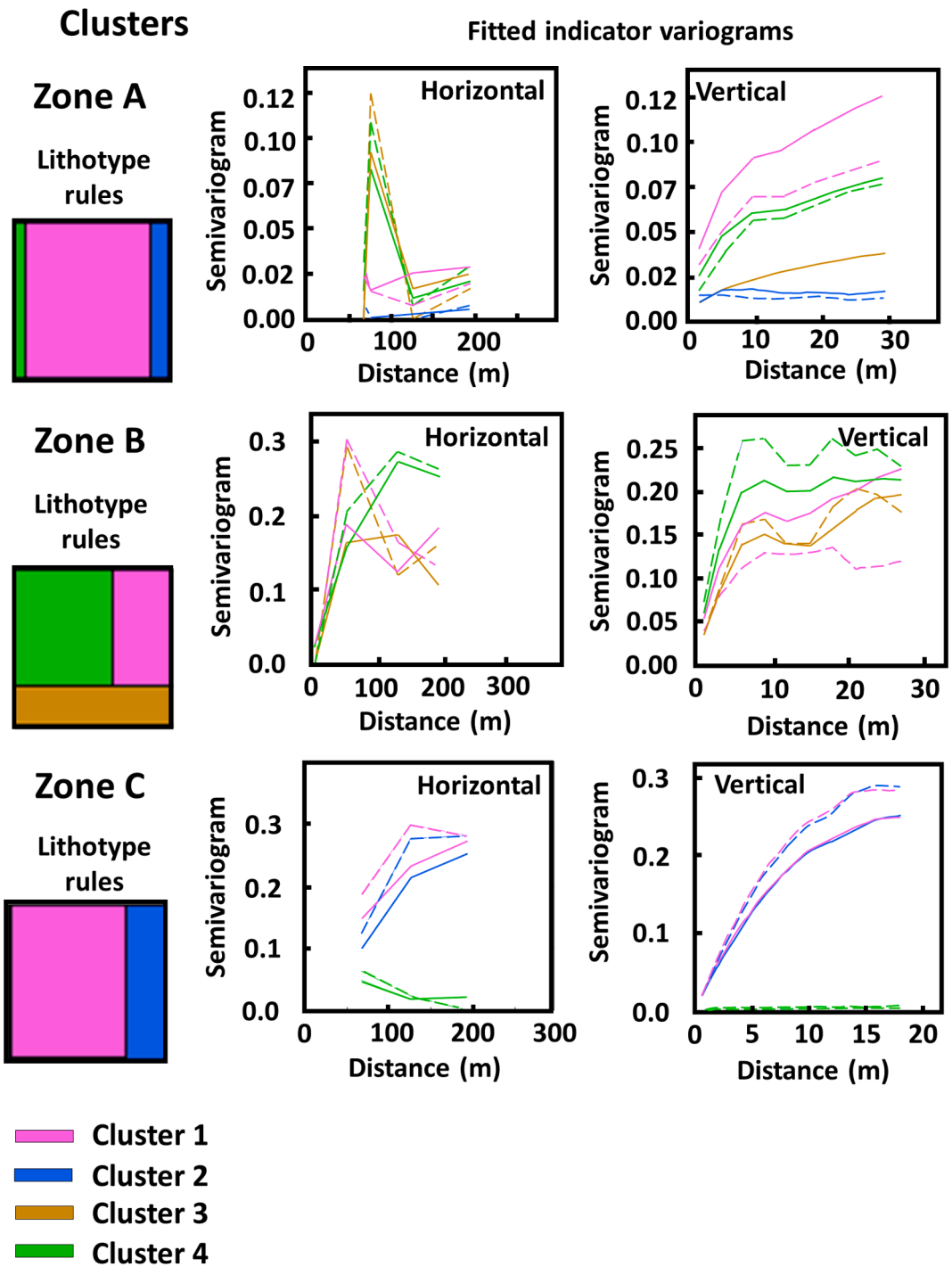

Fig. 10. Lithotype rule diagrams and indicator variograms along the omnidirectional horizontal and vertical directions of the four cluster numbers in the three zones shown in Fig. 7c. The dashed and solid lines denote the experimental and modeled semivariograms, respectively.

geologic model can be explained by these processes. The zoning reflects the dissemination of Cu and Fe in the stockwork and predominant distribution of Ca, Ba, Zn, Pb, and Fe in the exterior, as reported by Ohmoto (1996). Furthermore, similar features of the channel sediments with Na anomalies and sericite, illite, gypsum, and anhydrite fillings in the fluid paths (Singer and Kouda, 1983) were observed in the samples from weakly and moderately altered rocks in the study area.

Because the hydrothermal system is open to seawater recharge and hydrothermal fluid flow discharge (Pirajno, 2009), the inferred fault likely acts as a pathway of ambient cold seawater and causes mixing with hydrothermal fluids. This mixing may have induced the precipitation of polymetallic sulfides in association with the horizontal/stratiform subseafloor sulfide layer in zone B by means of a pH increase and temperature decrease of the fluids.

5. Conclusions

This study clarifies the geologic structure and 3D distribution of metal contents in the Hakurei Site, Izena Hole, in the middle Okinawa Trough, southwest Japan and interprets the mineralization process using two data-characterization methods, PCA and k-means clustering, and two geostatistical simulation methods, TBSIM and PGSIM. The most

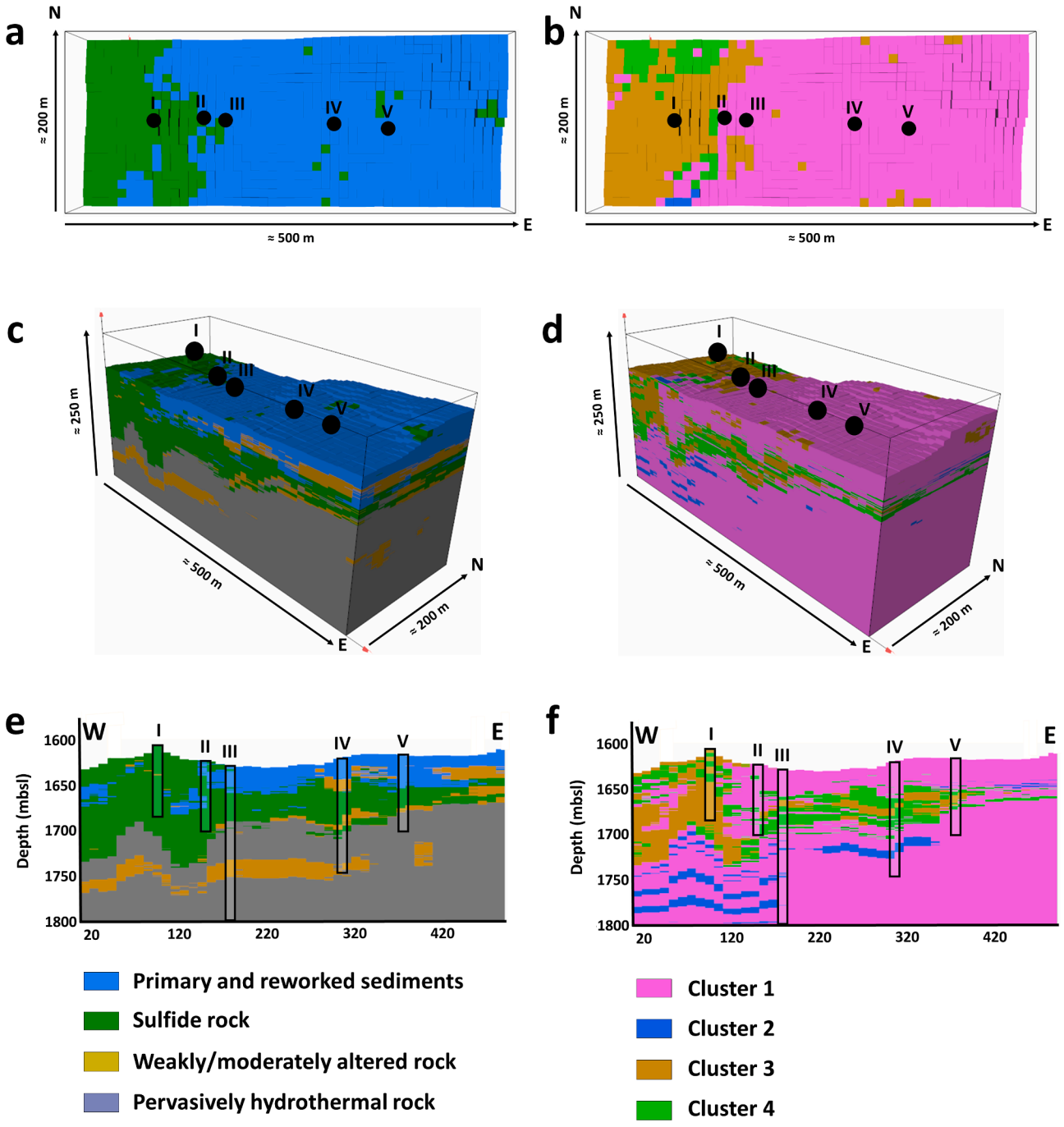

Fig. 11. Spatial modeling results of lithotype (a, c, and e on the left side) and cluster number (b, d, and f on the right side) by PGSIM: (a) and (b) are distributions on the seafloor; (c) and (d) are perspective views from the southeast; and (e) and (f) are E-W cross-sections with locations in Fig. 1c and the same location as Fig. 7b.

substantial hurdle was the sparse drill site data at only six locations along a given line. PCA was useful to select essential elements from the ICP-QMS data for characterizing the hydrothermal-originated mineralization. Eight elements, Zn, Pb, Cu, Ag, Ba, Cd, Mn, and Sn, were chosen for clustering. Most of the data are summarized by PC1 and the distribution of PC1 values was determined by TBSIM. High PC1 values suggests a stratiform mineralization zone and divides the study area into three zones depending on the similarity of PC1 values and lithotypes. PGSIM simulations of the lithotype and cluster number distributions were implemented independently with the zones. PGSIM honors category proportions and ordering relations through lithotype rule and transition matrix of category data.

The combination of data-characterization methods using PCA, k-means clustering, and geostatistical simulations proposed by this study can contribute to (i) construction of proper geologic and mineralization models and (ii) identification of hydrothermal fluid-flow systems and the accumulation mechanism of base metals in seafloor hydrothermal fields. Our next step is to incorporate geophysical logging data and more detailed XRD mineralogy data as supplementary information to improve the metal-content model and construct a fluid flow model by considering the PGSIM results.

Declaration of Competing Interest

The authors declare that they have no known competing financial interests or personal relationships that could have appeared to influence

Table 1
Correspondence of lithotypes to cluster numbers by a combination of the occurrence of lithotypes in each cluster number (Fig. 5c), median contents of eight elements used for PCA in each lithotype (Fig. 6), and PGSIM results of lithotype and cluster number (Fig. 11).

Lithotype	Cluster number	Content features of SMS-related polymetallic elements
Primary and reworked sediments	Cluster 1 in the shallow part	Low contents except Mn.
Sulfide rock	Cluster 3	High contents except Mn.
Weakly/moderately altered rock	Clusters 2 and 4	Cluster 4 is similar to Cluster 3, but has slightly higher contents of Ba and Mn; Cluster 2 shows the highest Mn content.
Pervasively altered rock	Cluster 1 in the deep part	Extremely low contents except Mn.

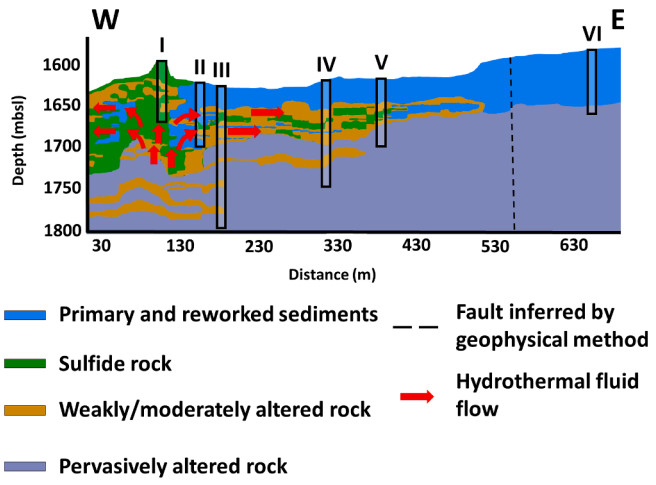

Fig. 12. Revised geologic model along an E-W cross-section with the same locations as Fig. 7b, 10e, and 10f by combining the PGSIM results of lithotypes and cluster numbers with the TBSIM results. Cluster numbers are renamed to corresponding lithotypes as shown in Table 1. Arrows show the interpreted hydrothermal fluid flows.

the work reported in this paper.

Acknowledgments

This work was supported by the Council for Science, Technology and Innovation (CSTI) and Cross-Ministerial Strategic Innovation Promotion Program (SIP), "Next-generation technology for ocean resources exploration" (Funding agency: Japan Agency for Marine-Earth Science and Technology, JAMSTEC). We thank the captain, crew, and on-board members of the cruise CK16-05 (*D/V Chikyu* Expedition 909). Sincere thanks are extended to the two anonymous reviewers for essential and constructive comments and suggestions that improved clarity of this manuscript largely.

References

Aitchison, J., 2002a. A concise guide to compositional data analysis. CDA Work. Girona 24, 73–81. https://doi.org/10.2307/4355794.
Aitchison, J., 2002a. Simplicial inference, In Viana, M.A.G., Richards, D.S.P. (Eds.), Algebraic methods in statistics and probability. Volume 287 of Contemporary mathematics series. American Mathematical Society, Providence, 1–22. https://doi.org/10.1090/conm/287/04772.
Arai, R., Kodaira, S., Yuka, K., Takahashi, T., Miura, S., Kaneda, Y., 2017. Crustal structure of the southern Okinawa Trough: Symmetrical rifting, submarine volcano, and potential mantle accretion in the continental back-arc basin. J. Geophys. Res. Solid Earth 122 (1), 622–641. https://doi.org/10.1002/2016JB013448.
Armstrong, M., Galli, A., Beucher, H., Le Loch, G., Renard, D., Doligez, B., Eschard, R., Geffroy, F. 2011. Plurigaussian Simulations in Geosciences. Berlin: Springer, pp. 176. https://doi.org/10.1007/978-3-642-19607-2.
Asakawa, E., Murakami, F., Tara, K., Saito, S., Tsukahara, H., Lee, S., 2018. Multi-stage seismic survey for Seafloor Massive Sulphide (SMS) exploration. 2018 Ocean. - MTS/IEEE Kobe Techno-Oceans. Ocean. Kobe 2018, 1–4. https://doi.org/10.1109/OCEANSKOBE.2018.8559188.
Carranza, E.J.M., 2011. Analysis and mapping of geochemical anomalies using logratio-transformed stream sediment data with censored values. J. Geochem. Explor. 110 (2), 167–185. https://doi.org/10.1016/j.gexplo.2011.05.007.
Cathles, L.M., 1983. An analysis of the hydrothermal system responsible for massive sulfide deposition in the Hokuroko basin of Japan. Econ. Geol. 5, 439–487.
Chilès, J.P., Delfiner, P., 2012. In: Geostatistics: Modeling Spatial Uncertainty. Wiley, New York, p. 699.
Cox, D.P., Singer, D.A., 1986. Mineral deposit models. U.S. Geol. Survey Bull. 1693, pp. 379. https://doi.org/10.3133/b1693.
Date, J., Watanabe, Y., Saedi, Y., 1983. Zonal alteration around the Fukazawa Kuroko deposits Akita Prefecture, northern Japan. Econ. Geol. Monogr. 5, 365–386.
Davis, J.C., 2012. In: Statistics and Data Analysis in Geology. Wiley, New York, p. 646.
de Sá, V.R., Koike, K., Goto, T. nori, Nozaki, T., Takaya, Y., Yamasaki, T. 2020. A Combination of Geostatistical Methods and Principal Components Analysis for Detection of Mineralized Zones in Seafloor Hydrothermal Systems. Natural Resource Research. https://doi.org/10.1007/s11053-020-09705-4.
Degens, E., Ross, D.A., 1969. In: Hot Brines and Heavy Metal Deposits in the Red Sea: A Geochemical and Geophysical Account. Springer, New York, p. 600.
Dempster, M., Dunlop, P., Scheib, A., Cooper, M., 2013. Principal component analysis of the geochemistry of soil developed on till in Northern Ireland. J. Maps 9, 373–389. https://doi.org/10.1080/17445647.2013.789414.
Deutsch, C.V., Journel, A.G., 1998. GSLIB: geostatistical software library and user's guide. Applied geostatistics series. New York: Oxford University Press.
Doyle, M.G., Allen, R.L., 2003. Subsea-floor replacement in volcanic-hosted massive sulfide deposits. Ore Geol. Rev. 23, 183–222. https://doi.org/10.1016/S0169-1368(03)00035-0.
Eldridge, C.S., Barton, P.B., Ohmoto, H., 1983. Mineral textures and their bearing on formation of the kuroko orebodies. Econ. Geol. Monogr. 5, 241–281.
Emery, X., Lantuéjoul, C., 2006. TBSIM: A computer program for conditional simulation of three-dimensional Gaussian random fields via the turning bands method. Comput. Geosci. 32, 1615–1628. https://doi.org/10.1016/j.cageo.2006.03.001.
Galley, A. G., Hannington, M., and Jonasson, I., 2007. Volcanogenic massive sulphide deposits, in Goodfellow, W.D. (ed.), Mineral deposits of Canada—A synthesis of major deposit-types, district metallogeny, the evolution of geological provinces, and exploration methods: Geological Association of Canada, Mineral Deposits Division, Special Publication, 5, 141–161.
German, C.R., Klinkhammer, G.P., Edmond, J.M., Mitra, A., Elderfield, H., 1990. Hydrothermal scavenging of rare earth elements in the ocean. Nature 345, 516–518. https://doi.org/10.1038/345516a0.
German, C.R., Campbell, A.C., Edmond, J.M., 1991. Hydrothermal scavenging at the Mid-Atlantic Ridge: Modification of trace element dissolved fluxes. Earth Planet. Sci. Lett. 107, 101–114. https://doi.org/10.1016/0012-821X(91)90047-L.
Glasby, G.P., Notsu, K., 2003. Submarine hydrothermal mineralization in the Okinawa Trough, SW of Japan: An overview. Ore Geol. Rev. 23, 299–339. https://doi.org/10.1016/j.oregeorev.2003.07.001.
Halbach, P., Nakamura, K., Wahsner, M., et al., 1989. Probable modern analogue of kuroko-type massive sulphide deposits in the Okinawa Trough back-arc basin. Nature 338, 496–499. https://doi.org/10.1038/338496a0.
Halbach, P., Pracejus, B., Marten, A., 1993. Geology and mineralogy of massive Sulfide rocks from the central Okinawa trough, Japan. Econ. Geol. 88 (8), 2210–2225. https://doi.org/10.2113/gsecongeo.88.8.2210.
Hannington, M., Jamieson, J., Monecke, T., Petersen, S., Beaulieu, S., 2011. The abundance of seafloor massive sulfide deposits. Geology 39, 1155–1158. https://doi.org/10.1130/G32468.1.
Hein, J.R., Mizell, K., Koschinsky, A., Conrad, T.A., 2013. Deep-ocean mineral deposits as a source of critical metals for high- and green-technology applications: Comparison with land-based resources. Ore Geol. Rev. 51, 1–14. https://doi.org/10.1016/j.oregeorev.2012.12.001.
Hemley, J.J., Montoya, J.W., Marinenko, J.W., Luce, R.W., 1980. Equilibria in the system Al_2O_2-SiO_2-H_20 and some general implications for alteration/mineralization processes. Econ. Geol. 75, 210–228.
Herzig, P.M., Hannington, M.D., 1995. Polymetallic massive sulfides at the modern seafloor, A review. Ore Geol. Rev. 10, 95–115. https://doi.org/10.1016/0169-1368(95)00009-7.
Hirata, N., Kinoshita, H., Katao, H., Baba, H., Kaiho, Y., Koresawa, S., Ono, Y., Hayashi, K., 1991. Report on DELP 1988 cruises in the Okinawa Trough Part 3. Crustal structure of the southern Okinawa Trough. Bull. Earthq. Res. Inst. 66, 37–70.
Hunger, L., Cosenza, B., Kimeswenger, S., Fahringer, T., 2015. Spectral turning bands for efficient Gaussian random fields generation on GPUs and accelerators. Concurr. Comput. https://doi.org/10.1002/cpe.3550.
Hutchinson, R.W., 1973. Volcanogenic sulfide deposits and their metallogenic significance. Econ. Geol. 68, 1223–1246. https://doi.org/10.2113/gsecongeo.68.8.1223.
Ishibashi, J.-I., Noguchi, T., Toki, T., Miyabe, S., Yamagami, S., Onishi, Y., Yamanaka, T., Yokoyama, Y., Omori, E., Takahashi, Y., Hatada, K., Nakaguchi, Y., Yoshizaki, M., Konno, U., Shibuya, T., Takai, K., Inagaki, F., Kawagucci, S., 2014. Diversity of fluid geochemistry affected by processes during fluid upwelling in active hydrothermal fields in the Izena Hole, the middle Okinawa Trough back-arc basin. Geochem. J. 48, 357–369. https://doi.org/10.2343/geochemj.2.0311.

Ishibashi, J.-I., Ikegami, F., Tsuji, T., Urabe, T., 2015. Hydrothermal activity in the Okinawa Trough Back-Arc Basin: Geological background and hydrothermal mineralization. In: Ishibashi, J.-.I. (Ed.), Subseafloor Biosphere Linked to Hydrothermal Systems: TAIGA Concept. Springer, Tokyo, pp. 281–304. https://doi.org/10.1007/978-4-431-54865-2.

Ishikawa, M., Sato, H., Furukawa, M., Kimura, M., Kato, Y., Tsugaru, R., Shimamura, K., 1991. Report on DELP 1988 cruises in the Okinawa Trough Part 6: petrology of volcanic rocks. Bull. Earthq Res. Inst. 66, 151–177.

Ishikawa, Y., Mikami, S., Hashimoto, K., 2004. Volcanic Rock Facies and Volcano Stratigraphy of the Lower to Middle Miocene in the Hokuroko District. Ministry Economy Trade and Industry, Japan (in Japanese).

Iwamori, H., Yoshida, K., Nakamura, H., Kuwatani, T., Hamada, M., Haraguchi, S., Ueki, K., 2017. Classification of geochemical data based on multivariate statistical analyses: Complementary roles of cluster, principal component, and independent component analyses. Geochem. Geophys. Geosyst. 18, 994–1012. https://doi.org/10.1002/2016GC006663.

Japan Oil, Gas and Metals National Corporation (JOGMEC), 2013. Confirmation of the large-scale submarine hydrothermal deposit in the Okinawa area (in Japanese). http://www.jogmec.go.jp/news/release/news_01_000009.html.

Japan Oil, Gas and Metals National Corporation (JOGMEC), 2016. Confirmed a resource amount of the submarine hydrothermal deposit at the Izena Hole in Okinawa is 7.4 million tons (in Japanese). http://www.jogmec.go.jp/news/release/news_06_000130.html.

Journel, A.G., Alabert, F.G., 1988. Focusing on spatial connectivity of extreme valued attributes: stochastic indicator models of reservoir heterogeneities. SPE Paper 18324.

Juliani, C., Ellefmo, S.L., 2018a. Resource assessment of undiscovered seafloor massive sulfide deposits on an Arctic mid-ocean ridge: Application of grade and tonnage models. Ore Geol. Rev. 102, 818–828. https://doi.org/10.1016/j.oregeorev.2018.10.002.

Juliani, C., Ellefmo, S.L., 2018b. Probabilistic estimates of permissive areas for undiscovered seafloor massive sulfide deposits on an Arctic Mid-Ocean Ridge. Ore Geol. Rev. 95, 917–930. https://doi.org/10.1016/j.oregeorev.2018.04.003.

Juliani, C., Ellefmo, S.L., 2019. Multi-scale quantitative risk analysis of seabed minerals: principles and application to seafloor massive sulfide prospects. Nat. Resour. Res. 28, 909–930. https://doi.org/10.1007/s11053-018-9427-y.

Kato, Y., Fujinaga, K., Nakamura, K., Takaya, Y., Kitamura, K., Ohta, J., Iwamori, H., 2011. Deep-sea mud in the Pacific Ocean as a potential resource for rare-earth elements. Nat. Geosci. 4 (8), 535–539. https://doi.org/10.1038/ngeo1185.

Kato, Y., Nakamura, K.-I., Iwabuchi, Y., Hashimoto, J., Kaneko, Y., 1989. Geology and topography in the Izena Hole of the middle Okinawa Trough—results of diving surveys in 1987 and 1988. JAMSTECTR Deep Sea Res. 5, 163–182 (in Japanese with English Abstract).

Kato, Y., Nakamura, K.-I., Iwabuchi, Y., Kawai, K., Seta, H., 1990. Topographic and geologic characteristics of the middle part of the Okinawa Trough revealed by seabeam survey around the Aguni Knoll studied with a submersible in 1986. JAMSTECTR Deep Sea Res. 5, 145–162 (in Japanese with English Abstract).

Kinoshita, M., Yamano, M., 1997. Hydrothermal regime and constraints on reservoir depth of the Jade site in Mid-Okinawa Trough inferred from heat flow measurements. J. Geogr. Res. 102 (B2), 3183–3194. https://doi.org/10.1029/96JB03556.

Maeda, K., Ito, M., Nakamura, K., Yamazaki, T., 1996. Submarine hydrothermal activity in the Izena Hole, Okinawa Trough. Abstract Volume of the 8th Annual Meeting of the Japan Society for Marine Surveys and Technology, 21 (in Japanese).

Marcotte, D., 2016. Spatial turning bands simulation of anisotropic non-linear models of coregionalization with symmetric cross-covariances. Comput. Geosci. 89, 232–238. https://doi.org/10.1016/j.cageo.2016.01.004.

Mariethoz, G., Renard, P., Cornaton, F., Jaquet, O., 2009. Truncated plurigaussian simulations to characterize aquifer heterogeneity. Ground Water 47, 13–24. https://doi.org/10.1111/j.1745-6584.2008.00489.x.

Martin, R.F., Piwinskii, A.J., 1972. Magmatism and tectonic settings. J. Geophys. Res. 77, 4966–4975.

Masuda, N., Okamoto, N., and Kawai, T., 2014. Sea-floor massive sulfide mining – its possibility and difficulties to emerge as a future business, in Drebenstedt, C., and Singhal, R. (Eds.), Mine Planning and Equipment Selection. Springer, Heidelberg, pp. 105–112. https://doi.org/10.1007/978-3-319-02678-7_11.

Matheron, G.H., Beucher, A., Galli, D., Guérillot, D., and Ravenne, C. 1987. Conditional simulation of the geometry of fluvio-deltaic reservoirs, in 62nd Annual Technical Conference and Exhibition of the Society of Petroleum Engineers, 591–599, SPE Paper 16753. Dallas. https://doi.org/10.2118/16753-MS.

Morozumi, H., Ishikawa, N., Chiba, M., Watanabe, K., Ogata, T., Takahashi, R., Ishibashi, J.-I., 2020. Characteristics of ore deposits for marine mineral resources investigated by JOGMEC since 2014. Shigen-Chishitsu 70, 53–65.

Nakada, S., 1986. Comparative study of chemistry of rocks from the Kirishima and the Daisen volcanic belts in Kyushu, southwest Japan. Bull. Volcanol. Soc. Japan 31, 95–110.

Nakashima, K., Sakai, H., Yoshida, H., Chiba, H., Tanaka, Y., Gamo, T., Tsunogai, U., 1995. Hydrothermal mineralization in the Mid-Okinawa Trough. Biogeochem. Process. Ocean Flux Western Pacific 487–508.

Nozaki, T., Ishibashi, J.-I., Shimada, K., Nagase, T., Takaya, Y., Kato, Y., Takai, K., 2016. Rapid growth of mineral deposits at artificial seafloor hydrothermal vents. Sci. Rep. 6, 22163. https://doi.org/10.1038/srep22163.

Nozaki, T., Nagase, T., Ushikubo, T., Shimizu, K., Ishibashi, J.-I., the D, V Chikyu Expedition 909 Scientists, 2021a. Microbial sulfate reduction plays an important role at the initial stage of subseafloor sulfide mineralization. Geology 49, 222–227.

Nozaki, T., Takaya, Y., Nagase, T., Yamasaki, T., Ishibashi, J.-I., Kumagai, H., Maeda, L., and CK16-05 Cruise Members, 2018. Subseafloor mineralization beneath hemipelagic sediments at the Izena Hole, middle Okinawa Trough, observed through the CK16-05 Cruise (Exp. 909). AGU Fall Meeting, Washington D.C., December.

Nozaki, T., Nagase, T., Takaya, Y., Yamasaki, T., Otake, T., Yonezu, K., Ikehata, K., Totsuka, T., Kitada, K., Sanada, Y., Yamada, Y., Ishibashi, J.-I., Kumagai, H., Maeda, L., The D/V Chikyu Expedition 909 Scientists, 2021b. Subseafloor sulphide deposit formed by pumice replacement mineralisation. Sci. Rep. 11, 8809. https://doi.org/10.1038/s41598-021-87050-z.

Ohmoto, H., 1996. Formation of volcanogenic massive sulfide deposits: the Kuroko perspective. Ore Geol. Rev. 10, 135–177.

Ohmoto, H., Takahashi, T., 1983. Geological, paleontological and tectonic studies, Pt 3. Submarine calderas and kuroko genesis. Econ. Geol. Monogr. 5, 39–54.

Olea, R.A., 1999. In: Geostatistics for Engineers and Earth Scientists. Kluwer Academic, Boston, p. 303.

Paravarzar, S., Emery, X., Madani, N., 2015. Comparing sequential Gaussian and turning bands algorithms for cosimulating grades in multi-element deposits. Comptes Rendus – Geoscience 347, 84–93. https://doi.org/10.1016/j.crte.2015.05.008.

Pawlowsky-Glahn, V., and Olea, R. A., 2004. Geostatistical analysis of compositional data. International Association for Mathematical Geosciences, Studies in Mathematical Geosciences, Oxford University Press, New York, pp. 181. https://doi.org/10.1016/j.gexplo.2015.12.010.

Pawlowsky-Glahn, V., Egozcue, J.J., Tolosana-Delgado, R., 2015. In: Modelling and Analysis of Compositional Data. Wiley, Chichester, p. 272.

Pirajno, F., 2009. In: Hydrothermal Processes and Mineral Systems. Springer, Berlin, p. 1250.

Poulsen, H., and Hannington, M., 1995. Auriferous volcanogenic sulfide deposits, in Eckstrand, O. R., Sinclair, W. D., and Thorpe, R. I. (Eds.), Geology of Canadian mineral deposit types: Geological Survey of Canada, Geology of Canada, 8, Geological Society of America, Decade of North American Geology, P1, pp. 183–196.

Pyrcz, M.J., Deutsch, C.V., 2014. In: Geostatistical Reservoir Modeling. Oxford University Press, New York, p. 433.

Robb, L., 2004. In: Introduction to Ore-Forming Processes. Oxford (Blackwell Publishing), p. 373 pp.

Sawkins, F.J., 1976. Massive sulphide deposits in relation to geotectonics, in Strong, D.F. (Ed.), Metallogeny and plate tectonics: Geological Association of Canada, Special Paper, 14, 221–240.

Shahi, H., 2017. Prediction of dispersed mineralization zone in depth using frequency domain of surface geochemical data. J. Mining Environ. 8 (3), 433–446. https://doi.org/10.22044/jme.2017.912.

Shanks, W.C.P., III, Thurston, R. 2012. Volcanogenic massive sulfide occurrence model, U.S. Geological Survey Scientific Investigations Report, 2010–5070–C. https://doi.org/10.1007/BF00206442.

Shinjo, R., Kato, Y., 2000. Geochemical constraints on the origin of bimodal magmatism at the Okinawa Trough, an incipient back-arc basin. Lithos 54, 117–137.

Shinjo, R., Chung, S.-L., Kato, Y., Kimura, M., 1999. Geochemical and Sr-Nd isotopic characteristics of volcanic rocks from the Okinawa Trough and Ryukyu Arc: Implications for the evolution of a young, intracontinental back arc basin. J. Geophys. Res. 104 (B5), 10591–10608.

Sibuet, J.-C., Letouzey, J., Barbier, F., Chavret, J., Foucher, J.-P., Hilde, T. W. C., Kimura, M., Chiao, L.-Y., Marsset, B., Muller, C., and Stéphan, J. F., 1987. Back arc extension in the Okinawa Trough. J. Geophys. Res., 92, 14041–14063. https://doi.org/10.1029/JB092iB13p14041.

Singer, D.A., Kouda, R., 1988. Integrating spatial and frequency information in the search for kuroko deposits of the Hokuroku District, Japan. Econ. Geol. 83 (1), 18–29. https://doi.org/10.2113/gsecongeo.83.1.18.

Singer, D.A., 2014. Base and precious metal resources in seafloor massive sulfide deposits. Ore Geol. Rev. 59, 66–72. https://doi.org/10.1016/j.oregeorev.2013.11.008.

Suzuki, R., Ishibashi, J.-I., Nakaseama, M., Konno, U., Tsunogai, U., Gena, K., Chiba, H., 2008. Diverse Range of Mineralization Induced by Phase Separation of Hydrothermal Fluid: Case Study of the Yonaguni Knoll IV Hydrothermal Field in the Okinawa Trough Back-Arc Basin. Resour. Geol. 58, 267–288. https://doi.org/10.1111/j.1751-3928.2008.00061.x.

Takaya, Y., Yasukawa, K., Kawasaki, T., et al., 2018. The tremendous potential of deep-sea mud as a source of rare-earth elements. Sci. Rep. 8, 5763. https://doi.org/10.1038/s41598-018-23948-5.

Tornos, F., Peter, J.M., Allen, R., Conde, C., 2015. Controls on the siting and style of volcanogenic massive sulphide deposits. Ore Geol. Rev. 68, 142–163. https://doi.org/10.1016/j.oregeorev.2015.01.003.

Totsuka, S., Shimada, K., Nozaki, T., Kimura, J.-I., Chang, Q., Ishibashi, J.-I., 2019. Pb isotope compositions of galena in hydrothermal deposits obtained by drillings from active hydrothermal fields in the middle Okinawa Trough determined by LA-MC-ICP-MS. Chem. Geol. 514, 90–104. https://doi.org/10.1016/j.chemgeo.2019.03.024.

Ueno, H., Hamasaki, H., Murakawa, Y., Kitazono, S., Takeda, T., 2003. Ore and gangue minerals of sulfide chimneys from the North Knoll. JAMSTEC J. Deep Sea Res. 22, 19–62.

Watanabe, M., Hoshino, K., Shiokawa, R., Takaoka, Y., Fukumoto, H., Shibata, Y., Oomori, T., 2006. Metallic mineralization associated with pillow basalts in the Yaeyama Central Graben, southern Okinawa Trough, Japan. JAMSTEC Rep. Res. Dev. 3, 1–8.

Yamasaki, T., 2017. Petrography and whole-rock major and trace element analyses of igneous rocks from Iheya North Knoll, middle Okinawa Trough, SIP Expedition CK14-04 (Exp. 907). J. Geol. Soc. Japan 123 (1), 23–29.
Yamasaki, T., 2018. The role of bimodal magmatism in seafloor massive sulfide (SMS) ore-forming systems at the iddle Okinawa Trough, Japan. Ocean Sci. J. 53 (2), 413–436. https://doi.org/10.1007/s12601-018-0031-1.
Zhou, S., Zhou, K., Wang, J., Yang, G., Wang, S., 2018. Application of cluster analysis to geochemical compositional data for identifying ore-related geochemical anomalies. Front. Earth Sci. 12 (3), 491–505. https://doi.org/10.1007/s11707-017-0682-8.